PCCP

PAPER

Cite this: *Phys. Chem. Chem. Phys.*, 2021, **23**, 13647

Chemical dynamics study on the gas-phase reaction of the D1-silylidyne radical (SiD; $X^2\Pi$) with deuterium sulfide (D_2S) and hydrogen sulfide (H_2S)†

Shane J. Goettl,[a] Srinivas Doddipatla,[a] Zhenghai Yang,[a] Chao He,[a] Ralf I. Kaiser,*[a] Mateus X. Silva,[b] Breno R. L. Galvão*[b] and Tom J. Millar*[c]

Received 15th April 2021,
Accepted 5th June 2021

DOI: 10.1039/d1cp01629f

rsc.li/pccp

The reactions of the D1-silylidyne radical (SiD; $X^2\Pi$) with deuterium sulfide (D_2S; X^1A_1) and hydrogen sulfide (H_2S; X^1A_1) were conducted utilizing a crossed molecular beams machine under single collision conditions. The experimental work was carried out in conjunction with electronic structure calculations. The elementary reaction commences with a barrierless addition of the D1-silylidyne radical to one of the non-bonding electron pairs of the sulfur atom of hydrogen (deuterium) sulfide followed by possible bond rotation isomerization and multiple atomic hydrogen (deuterium) migrations. Unimolecular decomposition of the reaction intermediates lead eventually to the D1-thiosilaformyl radical (DSiS) (p1) and D2-silanethione (D_2SiS) (p3) *via* molecular and atomic deuterium loss channels (SiD–D_2S system) along with the D1-thiosilaformyl radical (DSiS) (p1) and D1-silanethione (HDSiS) (p3) through molecular and atomic hydrogen ejection (SiD–H_2S system) *via* indirect scattering dynamics in barrierless and overall exoergic reactions. Our study provides a look into the complex dynamics of the silicon and sulfur chemistries involving multiple deuterium/hydrogen shifts and tight exit transition states, as well as insight into silicon- and sulfur-containing molecule formation pathways in deep space. Although neither of the non-deuterated species – the thiosilaformyl radical (HSiS) and silanethione (H_2SiS) – have been observed in the interstellar medium (ISM) thus far, astrochemical models presented here predict relative abundances in the Orion Kleinmann-Low nebula to be sufficiently high enough for detection.

1. Introduction

Ever since Langmuir devised the notion of isovalency, in which molecular entities with the same electronic structure and same number of valence electrons have similar chemistries,[1] the understanding of the key concepts surrounding molecular structure and chemical bonding along with the reactivity of isovalent species has improved our knowledge of the chemistries of main group XIV to XVI elements. Specifically, the chemistries of molecules containing main group XIV and XVI elements silicon (Si) and sulfur (S), which hold four and six valence electrons, respectively, have often been compared to their carbon (C) and oxygen (O) analogues,[2–5] with emphasis on, *e.g.*, the energies and stabilities of X = Y (X = C, Si; Y = O, S) double bonds.[6–11] While the carbon–oxygen double bond has been well-established for more than a century with typical bond lengths of 1.16 to 1.21 Å and bond strengths of about 700 to 900 kJ mol^{-1},[12,13] molecules containing double bonds between third period elements had been originally labeled as 'non-existent compounds'[14] until the early 1970s. Since then, various species comprising multiply bonded heavy elements have been synthesized[15–18] including members of the silanethione (R_2SiS) family. The first silanethione compound detected experimentally, the 2,4,6-triisopropylphenyl-2,4,6-tris[bis(trimethylsilyl)-methyl]phenylsilanethione molecule, was isolated by Suzuki *et al.*,[19] in which the product was stabilized by bulky substituents. More recently, the parent silanethione, H_2SiS (**5**) (Fig. 1), was characterized in a gas discharge of silane (SiH_4) and hydrogen sulfide (H_2S) using rotational spectroscopy by Thorwirth *et al.*[20] and by matrix isolation infrared spectroscopy by Liu *et al.*; the latter work also characterized the high energy isomer: thiohydroxysilylene (HSiSH; **6**, **7**).[5] Silanethione (H_2SiS; **5**) and singlet

[a] *Department of Chemistry, University of Hawai'i at Manoa, Honolulu, Hawaii 96822, USA. E-mail: ralfk@hawaii.edu*
[b] *Centro Federal de Educação Tecnológica de Minas Gerais, CEFET-MG, Av. Amazonas 5253, 30421-169 Belo Horizonte, Minas Gerais, Brazil. E-mail: brenogalvao@gmail.com*
[c] *School of Maths and Physics, Queen's University Belfast, University Road, Belfast BT7 1NN, Northern Ireland, UK. E-mail: Tom.Millar@qub.ac.uk*

† Electronic supplementary information (ESI) available. See DOI: 10.1039/d1cp01629f

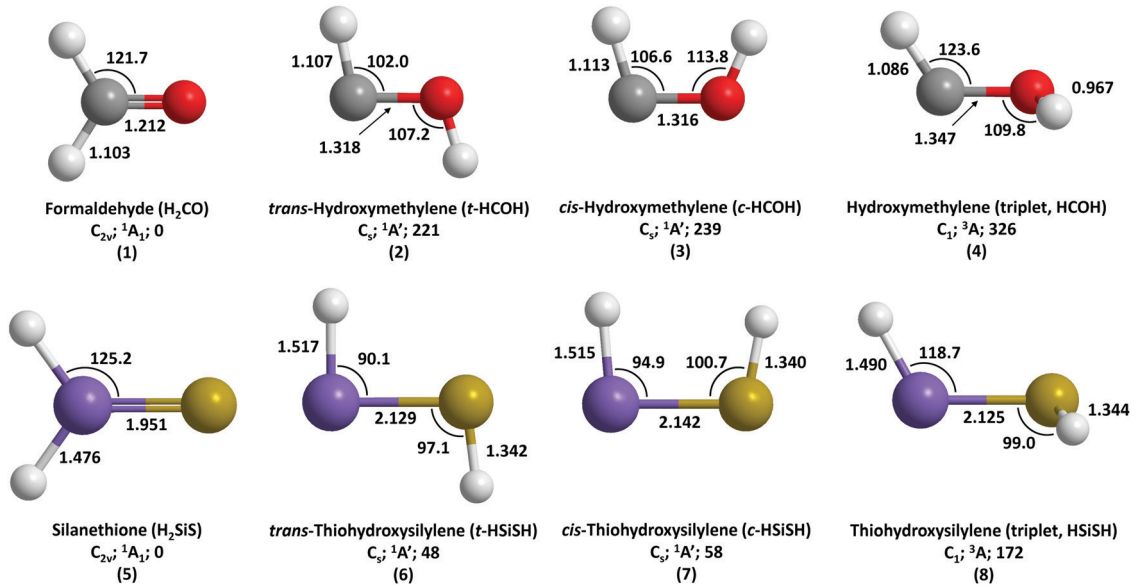

Fig. 1 Geometries, bond lengths (Å), bond angles (°), point groups, electronic ground state wavefunctions, and relative energies (kJ mol^{-1}) of formaldehyde (H_2CO), silanethione (H_2SiS), and their isomers. Elements are color coded as follows: carbon (grey); oxygen (red); silicon (purple); sulfur (yellow); hydrogen (white).

thiohydroxylsilylene (HSiSH; **6**, **7**) are the third period analogues of formaldehyde (H_2CO; **1**) and singlet hydroxymethylene (HCOH; **2**, **3**), respectively. These isovalent species have identical point groups and molecular structures (Fig. 1) with the greatest difference being their bond lengths.[21–24] This is primarily due to the larger atomic radius of silicon and its tendency to form weaker bonds than carbon, and the singlet–triplet gaps of the carbene-type species are reduced from 114 kJ mol^{-1} in case of thiohydroxysilylene (HSiSH; **6**–**8**) to 87 kJ mol^{-1} for hydroxymethylene (HCOH; **2**–**4**). Notably, silanethione (H_2SiS; **5**) and its *cis*/*trans*-thiohydroxysilylene isomers (HSiSH; **6**, **7**) are much closer in energy than formaldehyde (H_2CO; **1**) and hydroxymethylene (HCOH; **2**, **3**) of 48–58 kJ mol^{-1} compared to 221–239 kJ mol^{-1},[25,26] reinforcing the idea that silicon–sulfur double bonds are weaker than their carbon–oxygen counterparts.[7–9] Due to these differences, silanethione (H_2SiS; **5**) makes an ideal target of a directed synthesis to uncover information on the chemical reactivity and chemical dynamics of molecules containing both silicon and sulfur.

Besides chemical bonding and electronic structure, molecules incorporating silicon and sulfur are also of interest to the astrochemistry community. There have been over 200 molecules discovered in the interstellar medium (ISM) and circumstellar envelopes (CSEs), of which 13 contain silicon and 31 contain sulfur; the only interstellar molecule containing both silicon and sulfur is silicon monosulfide (SiS).[27] Silicon monosulfide has been observed in the CSEs of some 20 low to intermediate mass late-type carbon- and oxygen-rich Asymptotic Giant Branch (AGB) stars with mean fractional gas phase abundances of 3.1×10^{-6} and 2.7×10^{-7}, respectively.[28] SiS is particularly abundant in the CSE of the carbon-rich star IRC + 10216, where roughly one third of the molecules contain silicon and/or sulfur.[29] As the simplest silicon- and sulfur-containing closed-shell molecule after silicon monosulfide, the hydrogenated form – silanethione (H_2SiS; **5**) – is expected to be formed in interstellar environments. However, despite the high abundance of silicon monosulfide, silanethione (H_2SiS; **5**) has not been detected in deep space yet. An understanding of the driving mechanisms behind the formation of silanethione (H_2SiS; **5**) could elucidate the chemical conditions necessary for synthesis and give insight to why it has not yet been found in space.

Here, we unveil chemical dynamics of the bimolecular reaction of the D1-silylidyne radical (SiD; $X^2\Pi$) with deuterium sulfide (D_2S) and with hydrogen sulfide (H_2S) leading to D2/D1-silanethione (D_2SiS/DHSiS) along with the D1-thiosilaformyl radical (DSiS) under single-collision conditions utilizing crossed molecular beams experiments coupled with electronic structure calculations and astrochemical modeling. Hydrogen sulfide (H_2S) has been detected in star forming regions such as Orion-KL;[30] the silylidyne radical (SiH; $X^2\Pi$) has been tentatively detected in the same source.[31] While the silylidyne detection has not been confirmed,[32] a synthetic pathway to silanethione in the interstellar medium *via* the reaction of the silylidyne radical with hydrogen sulfide is plausible. Note that for the SiD/D_2S system, there are two reaction channels: the first leading to D2-silanethione (D_2SiS) *via* atomic deuterium (D) loss (reaction (1)) and the second forming D1-(iso)thiosilaformyl (DSiS/DSSi) radicals *via* molecular deuterium (D_2) loss (reaction (2)). In order to acquire additional information on the position of the atomic (H/D) and molecular (HD/H_2) hydrogen losses and the inherent reaction mechanisms, the reaction of the D1-silylidyne radical with hydrogen sulfide was also conducted (reactions (3)–(6)). This system also serves to explore the chemical bonding between silicon and sulfur by initiating a single-collision event between the D1-silylidyne radical transient and the simplest closed-shell sulfur hydride, hydrogen (deuterium) sulfide. Under these experimental conditions, successive reactions

and hydrogen-assisted isomerization processes, that would cause the nascent reaction products to change such as in bulk experiments, can be excluded,[33] and the species detected here represent the primary, unchanged reaction products.

$$SiD + D_2S \rightarrow D_2SiS + D \quad (1)$$

$$SiD + D_2S \rightarrow DSiS/DSSi + D_2 \quad (2)$$

$$SiD + H_2S \rightarrow HDSiS + H \quad (3)$$

$$SiD + H_2S \rightarrow H_2SiS + D \quad (4)$$

$$SiD + H_2S \rightarrow DSiS/DSSi + H_2 \quad (5)$$

$$SiD + H_2S \rightarrow HSiS/HSSi + HD \quad (6)$$

2. Experimental methods

Reactive scattering experiments of D1-silylidyne radicals (SiD; $X^2\Pi$) with deuterium sulfide (D_2S; 98.8% D atom; Sigma-Aldrich) and hydrogen sulfide (H_2S; ≥99.5%; Sigma-Aldrich) were conducted in a crossed molecular beams machine under single collision conditions.[34] The SiD/D_2S reaction was explored to unravel the chemical dynamics of the atomic (D) and molecular deuterium (D_2) loss pathways (reactions (1) and (2)), whereas the SiD/H_2S reaction was conducted to gain additional information on the position of atomic (H/D) and/or molecular hydrogen loss (HD/H_2) (reactions (3)–(6)). The setup consists of a 2.3 m^3 stainless steel box that is pumped by three 2.0 m^3 s^{-1} magnetically suspended compound molecular pumps (TG2003MCA, Osaka Vacuum) backed by a 0.010 m^3 s^{-1} scroll pump (XDS35, Boc Edwards) to the low 10^{-8} torr region; pressures of a few 10^{-9} torr are achievable by baking the main chamber. Housed in the main chamber are two source chambers and a triply differentially pumped detector that is rotatable in the scattering plane defined by both molecular beams. Each source chamber is pumped by a 2.0 m^3 s^{-1} (TG2003MCA, Osaka Vacuum) and 0.40 m^3 s^{-1} (TG420 MCAC, Osaka Vacuum) maglev pump backed by a 0.14 m^3 s^{-1} roots blower (RUVAC WSU 501, Leybold) and 0.008 m^3 s^{-1} scroll pump (GVSP30, Boc Edwards) to the mid 10^{-9} torr region.[35] The detector is composed of three differentially pumped regions: I and II reduce the gas load from the main chamber (with region II also containing the quadrupole mass spectrometer (QMS; QC 150, Extrel) and Daly-type[36] detector) and III contains a modified Brink-type[37] electron impact ionizer (80 eV) surrounded by a liquid nitrogen-cooled cold shield. Regions I, II, and III are pumped by two 0.43 m^3 s^{-1} (TG410MCA, Osaka Vacuum) and one 0.29 m^3 s^{-1} (TH261MCA, Osaka Vacuum) maglev pump, respectively; all pumps are backed by a 0.43 m^3 s^{-1} (TG403M, Osaka Vacuum) maglev and 0.005 m^3 s^{-1} scroll pump to reach pressures as low as 6×10^{-12} torr in region III; lower pressures of 8×10^{-13} torr are available by operating a 4 K cold head in region III. Neutral products that enter the detector are ionized and filtered by mass-to-charge (m/z) ratio in the QMS. Ions that passed through the filter were accelerated to an aluminum-coated stainless-steel target (−22.5 kV) creating a cascade of secondary electrons. These were directed to an aluminum-coated organic scintillator (BC-418, Saint Gobain) which generated a photon pulse that was collected by a photomultiplier tube (PMT; Model 8850, Burle) operating at −1.35 kV. The resulting signal passed through a discriminator set at 1.6 mV (Model F-100TD, Advanced Research Instruments) and was recorded by a multichannel scaler (MCS; Model 430, Stanford Research Systems), which files the signal in a series of 10.24 μs time bins to obtain the time-of-flight (TOF) spectra. An optimized pulse sequence was used to coordinate the data collection (Supplementary Note 1, ESI†). Note that the machine is equipped with an oxygen-free high conductivity (OFHC) copper shield located 7.4 ± 0.6 mm downstream from the chopper wheel and 8.1 ± 0.1 mm upstream from the interaction region to reduce the background pressure in the detector from straight-through molecules. The cold shield is cooled to 10 K *via* a cold head (Model 1020, CTI-Cryogenics) which further reduces pressure in the main chamber to the mid 10^{-9} torr region and also prevents straight-through molecules from reaching the ionizer.

A pulsed supersonic beam of D1-silylidyne radicals was produced *in situ* by laser ablation of a silicon rod (Si; 99.999%; Goodfellow Cambridge Limited) with the fourth harmonic output of a neodymium-doped yttrium aluminum garnet (Nd:YAG) laser (Quanta-Ray Pro 270, Spectra-Physics) operating at 30 Hz and 5–12 mJ and entraining the ablated species in a 1 : 1 gas mixture of neon (Ne; 99.999%; Airgas) and deuterium (D_2; 99.999% purity; ≥99.75% D atom; Linde) at a backing pressure of 3040 torr.[38–41] As a seeding gas, molecular deuterium (D_2) led to a low intensity of the D1-silylidyne beam and a significant fraction of metastable species, whereas addition of neon (Ne) was found to quench metastable D1-silylidyne radicals thus increasing D1-silylidyne availability for the crossed beam reaction. The 266 nm output was tightly focused by a plano-convex lens (PLCX-25.4-1030.2-UV-266, CVI) to a spot size of less than 1.5 mm^2 onto a silicon rod that was kept in helical motion by a motor (SP18074-3606).[42] In addition to acting as a seeding gas, the neon/deuterium mixture provided the reactant (D_2), most likely undergoing atomic deuterium abstraction by atomic silicon to form D1-silylidyne radicals.[38] Considering the isotopic abundances of silicon (92.2297% ^{28}Si; 4.6832% ^{29}Si; 3.0872% ^{30}Si) and that the fraction of D1-silylidyne to silicon in the primary beam was 8 ± 1%, the D1-silylidyne beam was optimized at m/z = 31 for ^{29}SiD to avoid overlap with silicon at m/z = 30 (^{30}Si). If D1-silylidyne radicals are formed in the $A^2\Delta$ excited state, their lifetime of about 500 ns causes them to decay to the ground state during the travel time of 39 μs to the interaction region.[43] The D1-silylidyne beam passed first through a stainless-steel skimmer located 18.0 ± 0.1 mm downstream of the primary pulsed valve nozzle, then through the slit of a chopper wheel located 11.6 ± 0.6 mm downstream of the skimmer, which selected a peak velocity (v_p) of 1142 ± 29 m s^{-1} and speed ratio (S) of 6.2 ± 1.1 (Table 1). A precision motion controller (MC 5005 S RS, Faulhaber) was coupled to the chopper wheel motor (2057S024B, Faulhaber). The signal period stability of 2083.3 ± 0.1 μs when operating at 480 Hz was

Table 1 Peak velocities (v_p) and speed ratios (S) of the D1-silylidyne (SiD; $X^2\Pi$), deuterium sulfide (D_2S; X^1A_1), and hydrogen sulfide (H_2S; X^1A_1) beams in addition to their collision energy (E_C) and center-of-mass angle (Θ_{CM})

Beam	v_p (m s^{-1})	S	E_C (kJ mol^{-1})	Θ_{CM} (°)
SiD ($X^2\Pi$)	1142 ± 29	6.2 ± 1.1		
D_2S (X^1A_1)	801 ± 21	12.8 ± 0.8	15.9 ± 0.9	40.8 ± 1.5
H_2S (X^1A_1)	805 ± 9	12.4 ± 0.1	15.6 ± 0.6	39.4 ± 1.0

ascertained with a digital oscilloscope (TDS 2024B, Tektronix). In the secondary source chamber, a pulsed deuterium sulfide beam (v_p = 801 ± 21 m s^{-1}; S = 12.8 ± 0.8) at a backing pressure of 550 torr passed a skimmer located 18.0 ± 0.1 mm downstream of the secondary pulsed valve nozzle before crossing perpendicularly with the D1-silylidyne beam. This resulted in a collision energy (E_C) of 15.9 ± 0.9 kJ mol^{-1} and center-of-mass (CM) angle (Θ_{CM}) of 40.8 ± 1.5°; experiments carried out with hydrogen sulfide (v_p = 805 ± 9 m s^{-1}; S = 12.4 ± 0.1) gave an E_C of 15.6 ± 0.6 kJ mol^{-1} and Θ_{CM} of 39.4 ± 1.0°.

Up to 2 × 10^6 TOF spectra were recorded at angles between 15 ≤ Θ ≤ 65° with respect to the D1-silylidyne beam (Θ = 0°), then integrated and normalized with respect to the CM angle intensity to give the laboratory angular distribution. To understand the dynamics of the reaction, the time- and angular-dependent laboratory data must be converted to the CM reference frame. This was done with a forward convolution routine accounting for apparatus performances, velocity spreads, and beam divergences to create user-defined CM translational energy ($P(E_T)$) and angular ($T(\theta)$) flux distributions, which were refined iteratively until an admissible fit of the laboratory data was attained.[44,45] The CM functions describe a product flux contour map which reveals the differential reactive cross section $I(u,\theta) \sim P(u) \times T(\theta)$ as intensity with respect to the angle θ and the CM velocity u.[46] The energy dependence of the reactive scattering cross-section of a barrierless, exoergic reaction is accounted for by utilizing the intermolecular, attractive dipole–dipole interaction potential between reactant species giving a reactive scattering cross-section of $E_T^{-2/3}$ energy dependence.[47]

3. Computational

The theoretical calculations were performed using the GAMESS-US[48] and MOLPRO[49] packages. Restricted wavefunctions were utilized in order to avoid spin contamination; no symmetry restrictions were imposed in the geometry optimizations. For a preliminary exploration of the potential energy surface (PES), density functional theory (DFT)[50] calculations were employed with the M06-2X[51] exchange and correlation functional along with the cc-pV(T+d)Z basis set.[52–54] At all obtained minima and transition states, the Hessian matrix was calculated to perform a vibrational analysis of all possible isotopologues here studied, from where all zero-point energy (ZPE) corrections were obtained at the M06-2X/cc-pV(T+d)Z level. Intrinsic reaction coordinate (IRC) calculations starting from all transition states (TS) were executed to ensure the correct connection paths. After the initial exploratory part, all structures were reoptimized using the more accurate coupled-cluster singles and doubles plus perturbative triples[55,56] (CCSD(T)) with the aug-cc-pV(T+d)Z basis set. At this level, the Hessian matrix was calculated and a vibrational analysis for the non-deuterated case only was performed, to make sure that the structures were still minima or transition states on the coupled-cluster PES. To further improve the energetic results, a single point energy using the explicitly correlated CCSD(T)-F12[57,58] method was employed. This highly accurate PES, termed as CCSD(T)-F12/aug-cc-pV(T+d)Z//CCSD(T)/aug-cc-pV(T+d)Z+ZPE(CCSD(T)/aug-cc-pV(T+d)Z), can be seen in the schematic representation given in Fig. S2 (ESI†) and it generally shows an accuracy within 4 kJ mol^{-1}.[59]

Finally, to obtain the ZPE corrected energies for the isotopic substitutions considered in this work, calculations of the vibrational frequencies using the M06-2X/cc-pV(T+d)Z level for all possible deuteration scenarios (the fully deuterated case, the case with one deuterium at each possible position, and the non-deuterated case) were conducted. These energies are therefore represented as CCSD(T)-F12/aug-cc-pV(T+d)Z//CCSD(T)/aug-cc-pV(T+d)Z+ZPE(M06-2X/cc-pV(T+d)Z). Note that for the non-deuterated case (SiH + H_2S), in which we have both the CCSD(T) and M06-2X values for the ZPE, a comparison shows that the maximum deviation between CCSD(T) and DFT computed ZPEs is of only 0.6 kJ mol^{-1}. For this reason, it was deemed unnecessary to calculate the ZPE of all isotopic variants using the highly expensive CCSD(T) method. All structures and parameters are listed in Table S1 (ESI†).

4. Astrochemical modeling

Since the well-defined conditions in a laboratory setting cannot fully replicate the complexity of the interstellar medium (ISM), astrochemical modeling is used to evaluate the effect of the reaction of silylidyne (SiH) with hydrogen sulfide (H_2S) on the observability of the atomic and molecular hydrogen loss products silanethione (H_2SiS) and the (iso)thiosilaformyl (HSiS/HSSi) radical. Silicon is heavily depleted from the gas phase in the interstellar medium with 90–99% of its cosmic abundance incorporated into refractory dust grains. In cold clouds, the remaining gas-phase silicon is accreted onto the icy mantles of the grains and likely converted to silane (SiH_4) consistent with the non-detection of silicon monoxide (SiO) to levels of a few times 10^{-12} relative to molecular hydrogen.[60,61] Silicon monoxide has been detected, however, in hot molecular cores[62] where ice mantles have been returned to the gas through heating and in shocked regions,[63] in some of which very high abundances indicate that the shock velocity is high enough to destroy grain cores. In these environments, reactive silicon species can be increased by up to six orders of magnitude in comparison to cold molecular clouds.[61,64] Here, the newly explored reaction of silylidyne radicals with hydrogen sulfide was incorporated in chemical models of three regions in the Orion Kleinmann-Low Nebula, *i.e.* the Orion 15.5 km s^{-1}

component (O15), the Orion Hot Core (OHC), and the Orion Plateau (OPl).[65] The physical conditions of these sources are presented in Table S2 (ESI†). Due to the 100 to 225 K temperature range of these sources, the model focuses on silane (SiH_4) and hydrogen sulfide (H_2S) that have been thermally desorbed along with grain ice mantles with initial fractional abundances of 2×10^{-7} and 2×10^{-6}, respectively, the latter value consistent with the abundance of hydrogen sulfide detected in the Orion Hot Core by Crockett *et al.* (2014).[66] The silylidyne radical can be formed from silane by a series of reactions involving cosmic ray-induced degradation and also by proton-transfer followed by dissociative recombination with electrons. The calculations of the fractional abundances begin at $t = 0$, when the ice mantles are injected into the gas phase, then follow the subsequent time-dependent chemistry up to 5×10^5 years using the DVODE package to solve the system of kinetics equations.[67] We have added over 40 gas-phase reactions to describe the chemistries of H_2SiS and HSiS using the trajectory scaling approximation[68] to calculate ion-neutral rate coefficients for the destruction of H_2SiS and HSiS/HSSi since their electric dipole moments are large, *i.e.* 2.67 D[20] and 2.044 D,[23] respectively. The newly formed molecules also react with radicals such as hydroxyl (OH) *via* neutral–neutral reactions. Our final reaction set is an extension of the UMIST Database for Astrochemistry[69] and consists of 6229 reactions among 472 species. In our calculations we adopt a total rate coefficient of 6×10^{-10} cm^3 s^{-1} for the silylidyne–hydrogen sulfide reaction and equal branching to H_2SiS and HSiS, consistent with our experimental measurements.

5. Results & discussion

5.1. Laboratory system

Due to the presence of atomic silicon (Si(^{3}P)) and D1-silylidyne (SiD; $X^2\Pi$) in the supersonic primary beam, both atomic silicon (Si(^{3}P)) and D1-silylidyne (SiD; $X^2\Pi$) react with deuterium sulfide (D_2S) and with hydrogen sulfide (H_2S). However, the chemical dynamics of the Si(^{3}P)–D_2S and Si(^{3}P)–H_2S systems were untangled earlier;[65,70] these experiments revealed reactive scattering signal at mass-to-charge ratios of 60 and 62 as well as 60 and 61, respectively, thus revealing the molecular hydrogen (deuterium) loss channel (reactions (7) and (9)) and the atomic hydrogen/deuterium elimination pathway (reactions (8) and (10)). Feasible mass combinations for these systems are compiled in Tables S3 and S4 (ESI†). It is important to highlight that for the SiD–D_2S/H_2S systems, due to the additional deuterium atom from the D1-silylidyne reactant, the reaction channels of the SiD–D_2S/H_2S systems can be discriminated from the Si–D_2S/H_2S reaction due to differences in mass-to-charge ratios (Tables S5 and S6, ESI†). The corresponding Newton diagrams and recoil circles of the heavy reaction products are presented in Fig. 2 and 3. This methodology has been applied earlier in our laboratory to extract the distinct chemical dynamics of the Si–SiH_4[71] and SiD–SiH_4[72] systems.

$$Si + D_2S \rightarrow SiS + D_2 \quad (7)$$

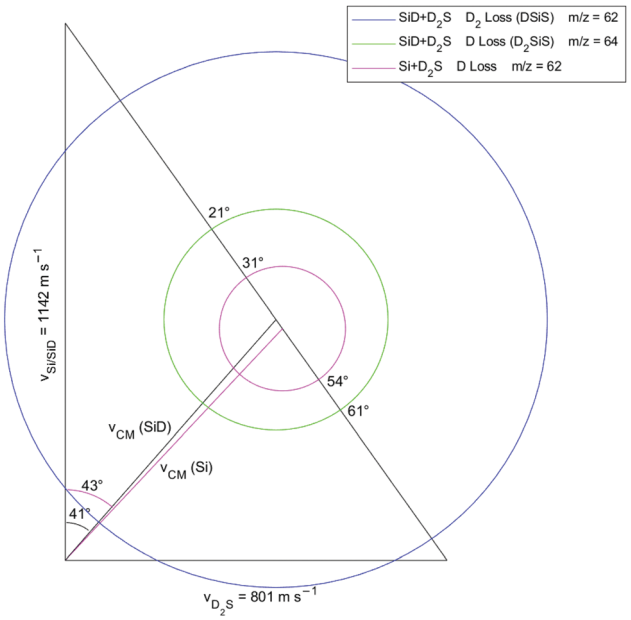

Fig. 2 Newton diagram for the reaction of ground state atomic silicon (Si(^{3}P)) with deuterium sulfide (D_2S) and of the D1-silylidyne radical (SiD; $X^2\Pi$) with deuterium sulfide (D_2S). The diagram is simplified by including only the most energetically favorable product channels for the D and D_2 loss pathways, while the full Newton diagram is shown in Fig. S3 (ESI†). Each Newton circle has a radius equal to the maximum CM recoil velocity of its corresponding heavy product.

$$Si + D_2S \rightarrow DSiS/DSSi + D \quad (8)$$

$$Si + H_2S \rightarrow SiS + H_2 \quad (9)$$

$$Si + H_2S \rightarrow HSiS/HSSi + H \quad (10)$$

5.1.1. SiD–D_2S system. Reactive scattering signal for the reaction of the D1-silylidyne radical (SiD; $X^2\Pi$) with deuterium sulfide (D_2S) was searched for at m/z = 62 and 64 to probe the molecular and atomic deuterium loss channels yielding – after ionization – signal for $D^{28}Si^{32}S^+$ (m/z = 62) and $D_2{}^{28}Si^{32}S^+$ (m/z = 64) (Fig. 4). Signal at m/z = 62 was observed; this signal could originate in principle from three sources: (i) $D^{28}Si^{32}S^+$ fragment ions from the dissociative electron impact ionization of the $D_2{}^{28}Si^{32}S$ isomer(s) of the atomic deuterium loss channel (reaction (1)), (ii) ionized reaction products of the molecular deuterium loss channel ($D^{28}Si^{32}S^+$) (reaction (2)), and (iii) ionized reaction products from the atomic deuterium loss channel of the Si–D_2S system ($D^{28}Si^{32}S^+$) (reaction (8)). Unfortunately, at m/z = 64 there was high background counts originating from dissociative electron impact ionization of deuterium disulfide (D_2S_2) – a minor impurity in the gas cylinder – yielding $^{32}S_2{}^+$; this background concealed any reactive scattering signal at m/z = 64. The TOF spectra (Fig. 4) at m/z = 62 show two distinct peaks with maxima at about 300–350 (fast component) and 500 μs (slow component) suggesting that more than one reaction channel is involved. These TOF spectra were normalized with respect to the CM angle and integrated to obtain the laboratory angular distribution (LAD), which spans from 19.25°

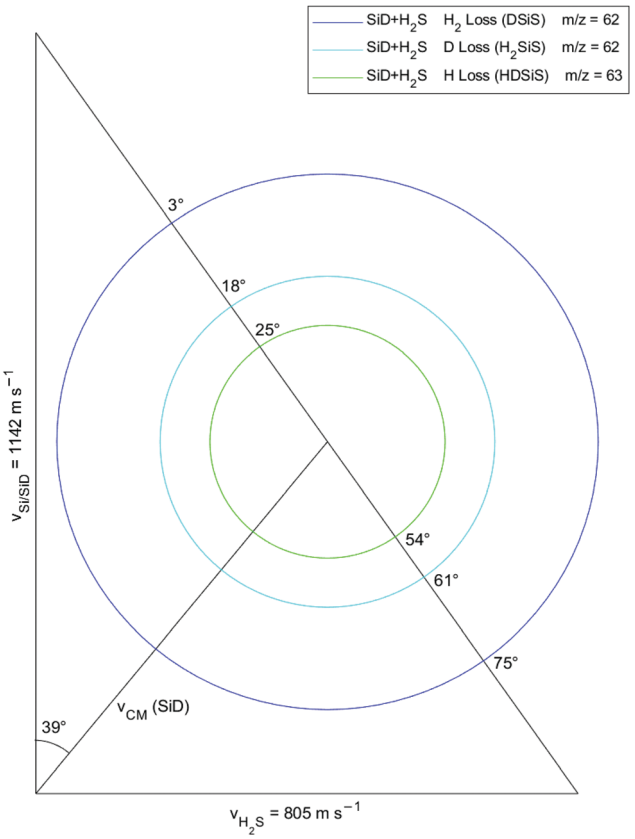

Fig. 3 Newton diagram for the reaction of the D1-silylidyne radical (SiD; $X^2\Pi$) with hydrogen sulfide (H_2S). The diagram is simplified by including only the most energetically favorable products for the H, D, and H_2 loss pathways, while the full Newton diagram is shown in Fig. S4 (ESI†). Each Newton circle has a radius equal to the maximum CM recoil velocity of its corresponding heavy product.

to 59.25°; this distribution is nearly symmetric around the CM angle. Additional information can be obtained by examining the Newton diagrams for the atomic and molecular deuterium loss channels for the SiD–D_2S system as well as for the atomic deuterium loss pathway of the Si–D_2S reaction (Fig. 2). The vectors along the *x*- and *y*-axes of the diagram correspond to the most probable velocities of the deuterium sulfide and silicon/D1-silylidyne reactant beams. Note that the atomic silicon is carried within the D1-silylidyne beam causing them to have the same velocity, but slightly different center-of-mass angles. The radii of the recoil circles represent the maximum CM velocity of the reactively scattered heavy products; each circle spans an angular range in which the corresponding product is expected to be observed by the detector. At m/z = 62, the LAD clearly depicts ion signal at angles outside the predicted range for the atomic deuterium loss channel and DSiS/DSSi heavy product of the Si–D_2S Newton circle (magenta); this finding reveals that the D and/or D_2 loss channels in the SiD–D_2S system are open.

5.1.2. SiD–H_2S system. Signal for the reaction of the D1-silylidyne radical (SiD; $X^2\Pi$) with hydrogen sulfide (H_2S) was scanned at m/z = 60 to 63 to probe for the atomic hydrogen loss ($HD^{28}Si^{32}S^+$, m/z = 63) (reaction (3)), the atomic deuterium loss ($H_2{}^{28}Si^{32}S^+$, m/z = 62; $H_2{}^{29}Si^{32}S^+/H_2{}^{28}Si^{33}S^+$, m/z = 63) (reaction (4)), molecular hydrogen loss ($D^{28}Si^{32}S^+$, m/z = 62; $D^{29}Si^{32}S^+/D^{28}Si^{33}S^+$, m/z = 63) (reaction (5)), and hydrogen deuteride loss ($H^{28}Si^{32}S^+$, m/z = 61; $H^{29}Si^{32}S^+/H^{28}Si^{33}S^+$, m/z = 62; $H^{30}Si^{32}S^+/H^{29}Si^{33}S^+/H^{28}Si^{34}S^+$, m/z = 63) (reaction (6)). These studies revealed the following findings. First, signal was observed at m/z = 63. Since no signal at m/z = 63 was observed in the Si–H_2S system, signal at m/z = 63 is unique to the SiD–H_2S reaction revealing the atomic hydrogen loss channel and formation of $HD^{28}Si^{32}S$ isomer(s). The TOF spectra at m/z = 63 (Fig. 5) show a single peak at about 500 μs with the nearly symmetric LAD spanning from 17.25° to 57.25°. This pattern is similar to the slow component of the SiD–D_2S system recorded at m/z = 62 suggesting that the dominating contributor to m/z = 62 in the SiD–D_2S system might indeed be dissociative electron impact ionization of the neutral D_2SiS product formed *via* the atomic deuterium loss.

Second, signal was also observed at m/z = 62. The corresponding TOFs (Fig. 6) distinctly show two peaks at 300–350 μs and 500 μs with the LAD ranging from 17.25° to 42.25°. This pattern mirrors the finding of the SiD–D_2S system discussed above: a fast component of the molecular and a slow component of the atomic deuterium loss channels with the latter originating from dissociative electron impact ionization of the neutral D_2SiS product. Therefore, in the SiD–H_2S system, signal at m/z = 62 supports the existence of the atomic hydrogen loss channel (HDSiS isomers) and of the molecular hydrogen loss pathway (DSiS isomers). Note that significant background counts at m/z = 62 closer to the secondary beam limited the experimentally recorded angular range. The aforementioned findings are also supported by the Newton diagram of the SiD–H_2S system depicting the H, D, and H_2 loss channels (Fig. 3). The angular range of the hydrogen atom loss recoil circle matches the LAD for m/z = 63 providing additional evidence for the formation of the $HD^{28}Si^{32}S$ isomer(s), *i.e.* at least the $HD^{28}Si^{32}S$ species. The LAD for m/z = 62 has a similar shape as m/z = 63 prior to a noticeable broadening at lower angles; this suggests additional contributions from the molecular hydrogen loss channel forming DSiS isomer(s) due to its wider recoil circle. This finding also correlates with the TOF spectra, *i.e.* the presence of two distinct peaks. For m/z = 62, this is once again indicative that products are formed from the molecular hydrogen loss pathway (fast signal) and the H and/or D loss pathways (slow signal). Finally, it is important to note that signal was also observed at m/z = 60 and 61 at the CM angle; however, the data were ill constrained due to the uncertainty in multichannel fits.

5.2. Center-of-mass system

To elucidate the chemical dynamics of the SiD–D_2S/H_2S systems, the laboratory data were transformed from the laboratory into the CM reference frame to obtain the $P(E_T)$ and $T(\theta)$.

5.2.1. SiD–D_2S system. First, for the SiD–D_2S system, the slow, more intense contribution of the TOF spectra (Fig. 4) at m/z = 62 could be replicated through a single-channel fit for the reaction SiD (30 amu) + D_2S (36 amu) → D_2SiS (64 amu) + D (2 amu)

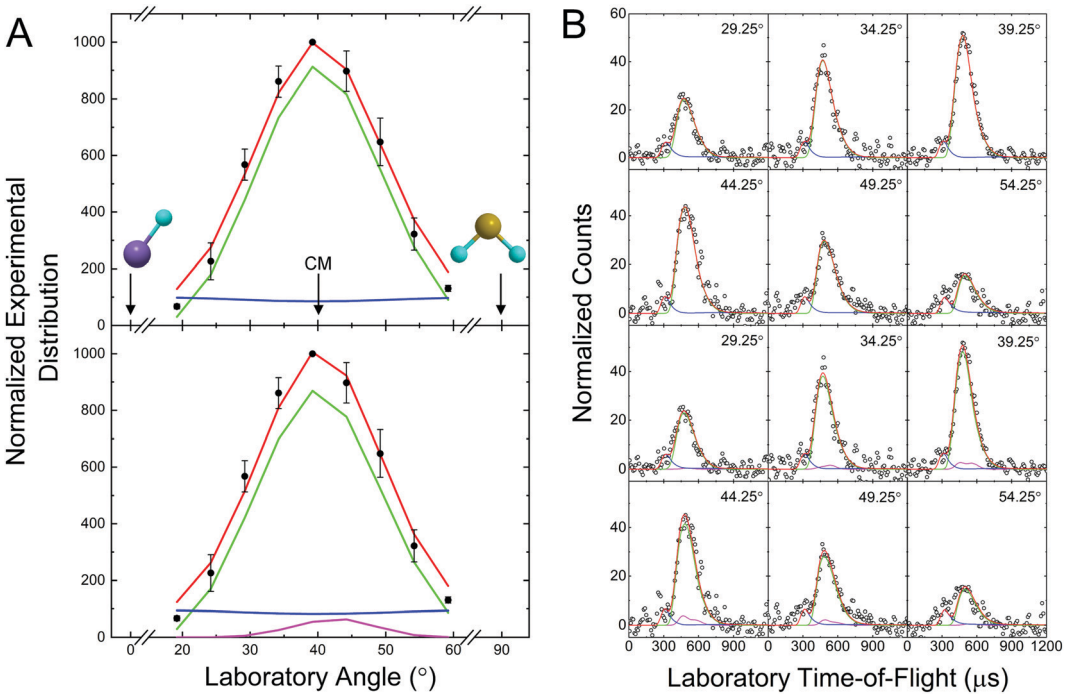

Fig. 4 Laboratory angular distribution (A) and time-of-flight (TOF) spectra (B) recorded at m/z = 62 for the reaction of deuterium sulfide (D_2S) with the D1-silylidyne radical (SiD; $X^2\Pi$). The data were fit with two channels (top) and with three channels (bottom). The two channels in the top fits correspond to $DSiS^+$ at m/z = 62 (dark blue) and fragmentation of atomic deuterium (D) from D_2SiS^+ at m/z = 64 (green). The three channels in the bottom fits correspond to $DSiS^+$ at m/z = 62 (dark blue), fragmentation of atomic deuterium (D) from D_2SiS^+ at m/z = 64 (green), and also $DSiS^+$ at m/z = 62 (magenta) from the reaction of ground state atomic silicon ($Si(^3P)$) with deuterium sulfide (D_2S). CM represents the center-of-mass angle, and 0° and 90° define the directions of the D1-silylidyne and deuterium sulfide beams, respectively. The black circles depict the experimental data, colored lines the fits (red corresponding to the total fit), and error bars the 1σ standard deviation.

with m/z = 62 originating from dissociative electron impact ionization of the nascent product ions at m/z = 64 (Fig. 7). Second, the fast peak was fit *via* a single channel of the reaction SiD (30 amu) + D_2S (36 amu) → DSiS (62 amu) + D_2 (4 amu). These two channels were able to replicate the experimental data at m/z = 62 with overall branching ratios[73,74] of 43 ± 8% and 57 ± 8% for the atomic and molecular deuterium loss channels, respectively (Fig. 4 (top)). However, recall that m/z = 62 could also be a contributor from the Si–D_2S reaction,[65] *i.e.* the formation of $D^{28}Si^{32}S$ isomers. To objectively account for this possibility, we also attempted to fit the LAD distribution at m/z = 62 with three components (Fig. 4 (bottom)) extracting the CM functions of the deuterium loss channel (m/z = 62) for the Si–D_2S system from Doddipatla *et al.*[65] Here, we could add contributions from the Si–D_2S reaction of up to 2 ± 1% and overall fractions for the SiD–D_2S system of 44 ± 7% and 54 ± 10% for the atomic and molecular deuterium loss channels, respectively.

For the slow channel (atomic deuterium loss) forming D_2SiS isomer(s), the $P(E_T)$ (Fig. 7A) exhibits a maximum translational energy, E_{max}, of 64 ± 17 kJ mol^{-1} for those products without internal excitation. Conservation of energy dictates that $E_{max} = E_C - \Delta_r G$ where E_C is the collision energy of the reaction (15.9 ± 0.9 kJ mol^{-1}) and $\Delta_r G$ the reaction energy. This reveals that the reaction to form D_2SiS plus atomic deuterium is exoergic by −48 ± 18 kJ mol^{-1}. The $P(E_T)$ depicts a peak at 14 kJ mol^{-1} suggesting that there is a tight exit transition state from the decomposing D_3SiS intermediate(s) to the D_2SiS plus D products. The best fit $T(\theta)$ (Fig. 7B) shows that the products have equal scattering probability in all directions; further, a forward–backward symmetry is clearly observable. These findings suggest indirect scattering dynamics through D_3SiS intermediate(s), with lifetimes longer than the rotational period(s). Second, the $P(E_T)$ for the fast channel (molecular deuterium loss) leading to DSiS/DSSi isomer(s) (Fig. 8A) shows an E_{max} of 162 ± 21 kJ mol^{-1}, revealing that the reaction to form DSiS/DSSi plus D_2 is exoergic by −146 ± 22 kJ mol^{-1}. The $P(E_T)$ depicts a peak at 119 kJ mol^{-1} indicating a tight exit transition state and significant electron redistribution from the decomposing D_3SiS intermediate(s) to the DSiS/SiSD plus D_2 products. The $T(\theta)$ (Fig. 8B) shows forward–backward symmetry and that the products have equal scattering probability in all directions, which suggests indirect scattering dynamics through long-lived D_3SiS intermediate(s). To summarize, the SiD–D_2S system revealed the existence of at least two channels: (i) D_2SiS (64 amu) + D (2 amu) and (ii) DSiS (62 amu) + D_2 (4 amu) with branching ratios of 43 ± 8% and 57 ± 8%, respectively.

5.2.2. SiD/H_2S system. For the SiD–H_2S system, the TOFs at m/z = 63 (Fig. 5) were fit with a single channel corresponding to the reaction SiD (30 amu) + H_2S (34 amu) → HDSiS (63 amu) + H (1 amu) (Fig. 9). The CM functions used were nearly identical to those for the deuterium loss channel fit of the slow peak for the SiD–D_2S system. The $P(E_T)$ (Fig. 9A) shows an E_{max} of

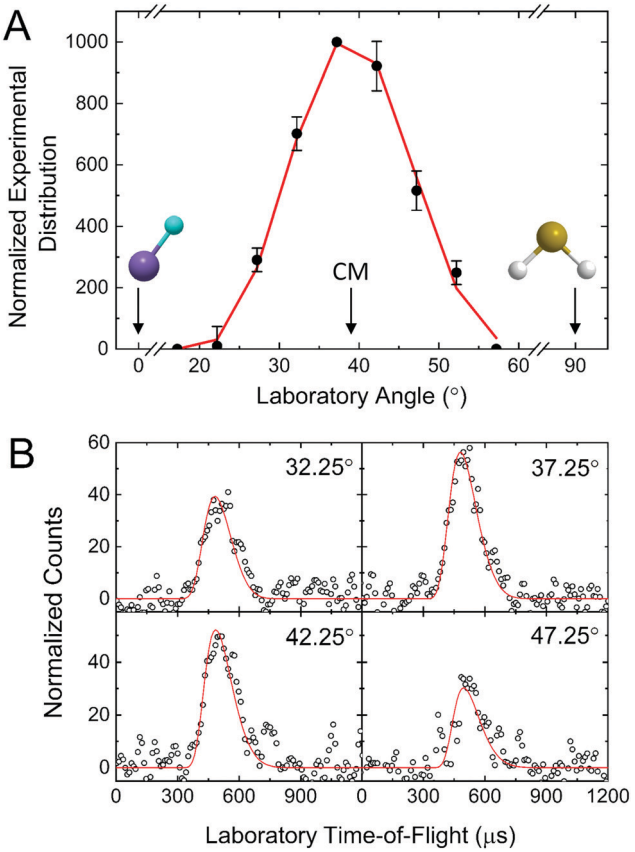

Fig. 5 Laboratory angular distribution (A) and TOF spectra (B) for the reaction of hydrogen sulfide (H_2S) with the D1-silylidyne radical (SiD; $X^2\Pi$) recorded at m/z = 63, which corresponds to the ionized product $HDSiS^+$. CM represents the center-of-mass angle, and 0° and 90° define the directions of the D1-silylidyne and hydrogen sulfide beams, respectively. The black circles depict the experimental data, red lines the fit, and error bars the 1σ standard deviation.

63 ± 13 kJ mol^{-1} revealing a reaction energy of −47 ± 14 kJ mol^{-1}; the distribution further reveals a maximum of 18 kJ mol^{-1} suggesting an exit barrier from H_2DSiS intermediate(s) to form the HDSiS/HSiSD/DSiSH products. The $T(\theta)$ (Fig. 9B) is nearly isotropic and forward–backward symmetric implying an indirect reaction with a long-lived intermediate.

The TOFs at m/z = 62 had a fast and slow component (Fig. 6). The slow peak could be fit with identical CM functions as those used for the TOFs at m/z = 63 (Fig. 9) indicating that the slow component of the TOFs at m/z = 62 originates from dissociative electron impact ionization of the m/z = 63 products (HDSiS) formed *via* SiD (30 amu) + H_2S (34 amu) → HDSiS (63 amu) + H (1 amu). It is important to note that in principle, the slow component of m/z = 62 could also originate from the formation of H_2SiS plus atomic deuterium: SiD (30 amu) + H_2S (34 amu) → H_2SiS (62 amu) + D (2 amu); this fit is shown in Fig. 6 (middle). Finally, a third fit utilizing both the dissociative electron impact ionization channel of m/z = 63 and the atomic deuterium pathway leading to H_2SiS (62 amu) could reproduce the experimental data with branching ratios of 75 ± 4% and 25 ± 4%, respectively (Fig. 6 (bottom)). Overall, the slow peak at m/z = 62 can originate from the HDSiS (63 amu) + H (1 amu) (dissociative electron impact ionization) and/or H_2SiS (62 amu) + D (2 amu). Hereafter, the fast component was fit with a single channel corresponding to the SiD (30 amu) + H_2S (34 amu) → DSiS (62 amu) + H_2 (2 amu) channel. Fig. 10A shows the $P(E_T)$ for the H_2 loss channel, which results in an E_{max} of 162 ± 21 kJ mol^{-1} and reaction energy of −146 ± 22 kJ mol^{-1}; this data is within the error range identical to that of the D_2 loss channel from the SiD–D_2S reaction: SiD (30 amu) + D_2S (36 amu) → DSiS (62 amu) + D_2 (4 amu). Further, the $P(E_T)$ shows a maximum at 124 kJ mol^{-1} indicating once again a tight exit transition state from H_2DSiS intermediates to the DSiS/SiSD products. The $T(\theta)$ (Fig. 10B) is also isotropic and forward–backward symmetric suggesting long-lived intermediate(s) and indirect scattering dynamics. To summarize, the SiD–H_2S system provided evidence on the existence of at least two channels: (i) DSiS (62 amu) + H_2 (2 amu) and (ii) HDSiS (63 amu) + H (1 amu) and possibly H_2SiS (62 amu) + D (2 amu) with branching ratios of 72 ± 9%, 21 ± 5%, and 7 ± 3%, respectively.

5.3. Potential energy surface

The experimental results and electronic structure calculations can be merged to obtain further information on the dynamics of the reactions. The calculated PES for the SiD–D_2S system is shown in Fig. 11. The D1-silylidyne radical undergoes barrierless addition to one of the lone electron pairs of sulfur of the deuterium sulfide to form intermediate **i1a** and/or **i1b**; these two intermediates may isomerize to one another *via* a bond rotation through a transition state at −54 kJ mol^{-1} relative to the separated reactants. Intermediate **i1a** can form product **p2** *via* molecular deuterium (D_2) loss through a tight transition state or isomerizes by atomic deuterium migration to **i2** through a tight transition state located 31 kJ mol^{-1} above **i1a**; intermediate **i1b** also isomerizes to **i2** through a barrier 28 kJ mol^{-1} above **i1b**. At this point, **i2** can isomerize by deuterium migration to **i3** or forms products **p2** (D_2 loss; tight exit transition state), **p3** (D loss; exit barrier), **p4** (D loss; no exit barrier) or **p5** (D loss; no exit barrier). From **i3**, **p1** and/or **p3** are accessible; the pathway from **i3** to **p3** is barrierless as shown in Fig. S5 (ESI†). The experimentally derived reaction energy from the D and D_2 loss channels −48 ± 18 kJ mol^{-1} and −146 ± 22 kJ mol^{-1} matches that of **p3** (D_2SiS; −39 ± 4 kJ mol^{-1}) and at least **p1** (DSiS; −131 ± 4 kJ mol^{-1}), respectively, whereas their isomers lie outside their respective error ranges. However, **p2**, **p4**, and **p5** are still possible contributors, as the E_{max} for each can cloak their contribution in the low energy portion of the $P(E_T)$. To summarize, at least **p1** and **p3** are suggested to be formed *via* atomic and molecular deuterium loss, respectively, leading to D2-silanethione (D_2SiS) along with the D1-thiosilaformyl radical (DSiS).

The PES for the SiD–H_2S system is shown in Fig. 12; this surface exhibits the same reaction pathways as the fully deuterated case plus additional routes due to the partial deuteration of the system. In this case there are three additional intermediates (**i1b′**, **i1a′**, and **i2′**), which are related to **i1b**, **i1a**, and **i2** due to the deuterium atom location, as well as additional

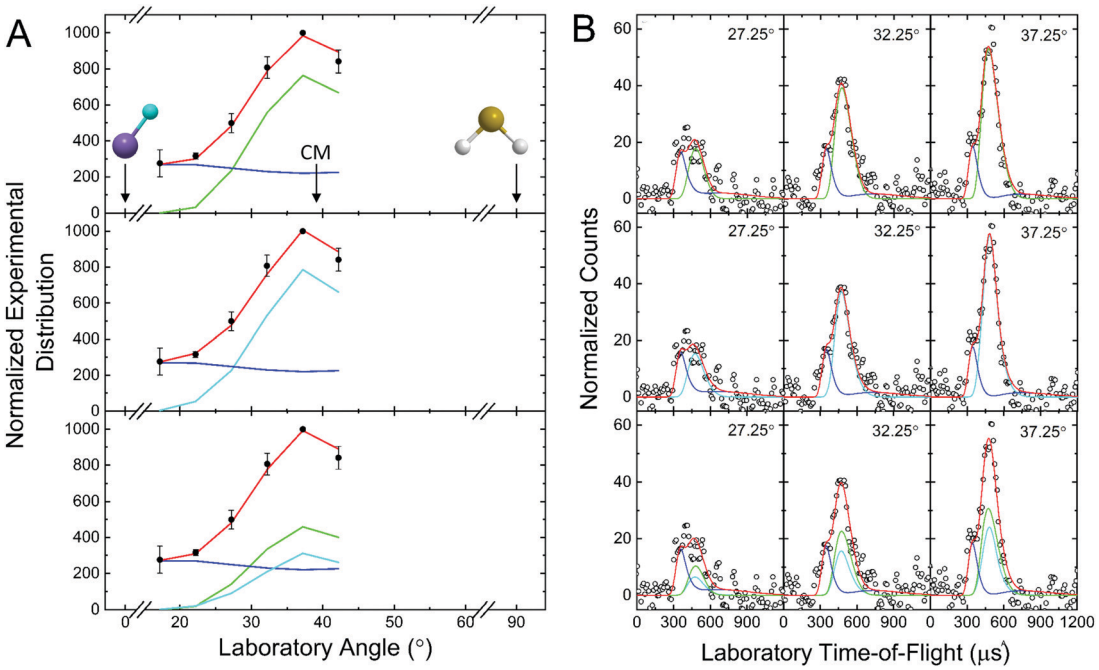

Fig. 6 Laboratory angular distribution (A) and time-of-flight (TOF) spectra (B) recorded at m/z = 62 for the reaction of hydrogen sulfide (H_2S) with the D1-silylidyne radical (SiD; $X^2\Pi$). There are three fits for the data: first with two channels corresponding to $DSiS^+$ (dark blue) at m/z = 62 and fragmentation of atomic hydrogen (H) from $HDSiS^+$ (green) at m/z = 63 (top); second with two channels corresponding to $DSiS^+$ (dark blue) at m/z = 62 and H_2SiS^+ (light blue) at m/z = 62 (middle); and third with all three channels (bottom). CM represents the center-of-mass angle, and 0° and 90° define the directions of the D1-silylidyne and hydrogen sulfide beams, respectively. The black circles depict the experimental data, colored lines the fits (red corresponding to the total fit), and error bars the 1σ standard deviation.

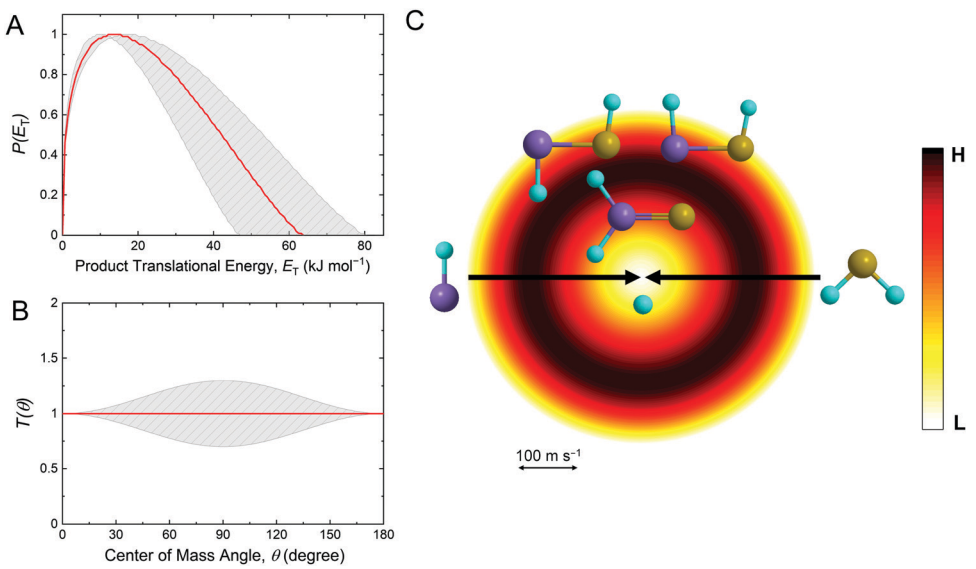

Fig. 7 CM translational energy (A) and angular (B) flux distributions, as well as the associated flux contour map (C) leading to the formation of D_2SiS/DSiSD (m/z = 64) plus atomic deuterium in the reaction of the D1-silylidyne radical (SiD; $X^2\Pi$) with deuterium sulfide (D_2S). Red lines define the best-fit functions while shaded areas denote the error limits. The flux contour map represents the flux intensity of the reactively scattered products as a function of the product velocity (u) and CM scattering angle (θ), and the color bar indicates the flux gradient from high (H) to low (L) intensity. Atoms are colored as follows: silicon (purple); sulfur (yellow); deuterium (light blue).

products (**p1**′, **p2**′, **p3**′, **p4**′, **p4**″, **p5**′, **p5**″) since H, D, H_2, or HD losses could be open. Here, **p1** and **p1**′ are formed *via* the similar pathway as in the fully deuterated case, with **p1** formed through molecular hydrogen (H_2) loss and **p1**′ formed through hydrogen deuteride (HD) loss. The reaction energy found from the $P(E_T)$ for the H_2 loss channel is -146 ± 22 kJ mol^{-1},

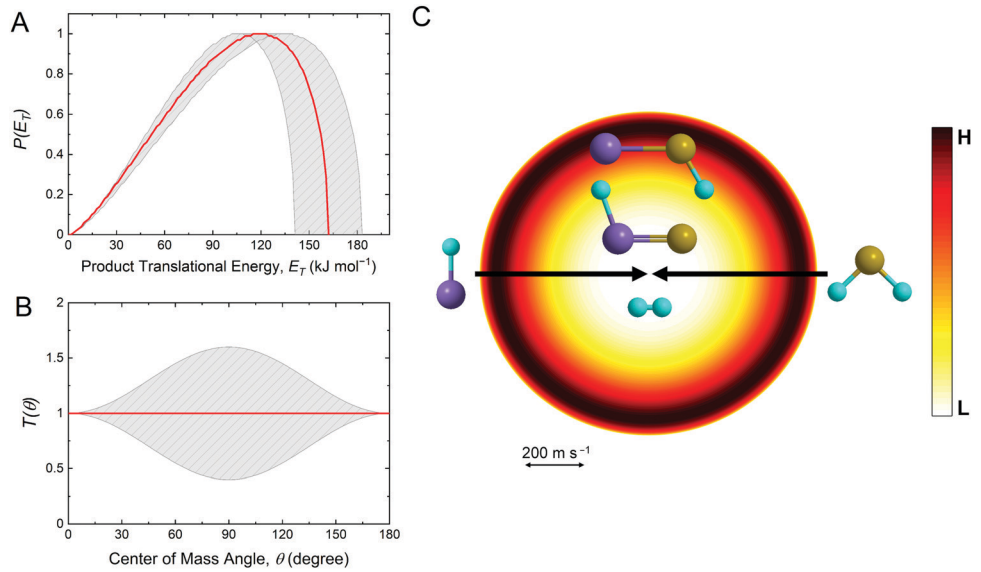

Fig. 8 CM translational energy (A) and angular (B) flux distributions, as well as the associated flux contour map (C) leading to the formation of the D1-(iso)thiosilaformyl (DSiS/SiSD) radical (m/z = 62) plus molecular deuterium in the reaction of D1-silylidyne radical (SiD; $X^2\Pi$) with deuterium sulfide (D_2S). Red lines define the best-fit functions while shaded areas denote the error limits. The flux contour map represents the flux intensity of the reactively scattered products as a function of the product velocity (u) and CM scattering angle (θ), and the color bar indicates the flux gradient from high (H) to low (L) intensity. Atoms are colored as follows: silicon (purple); sulfur (yellow); deuterium (light blue).

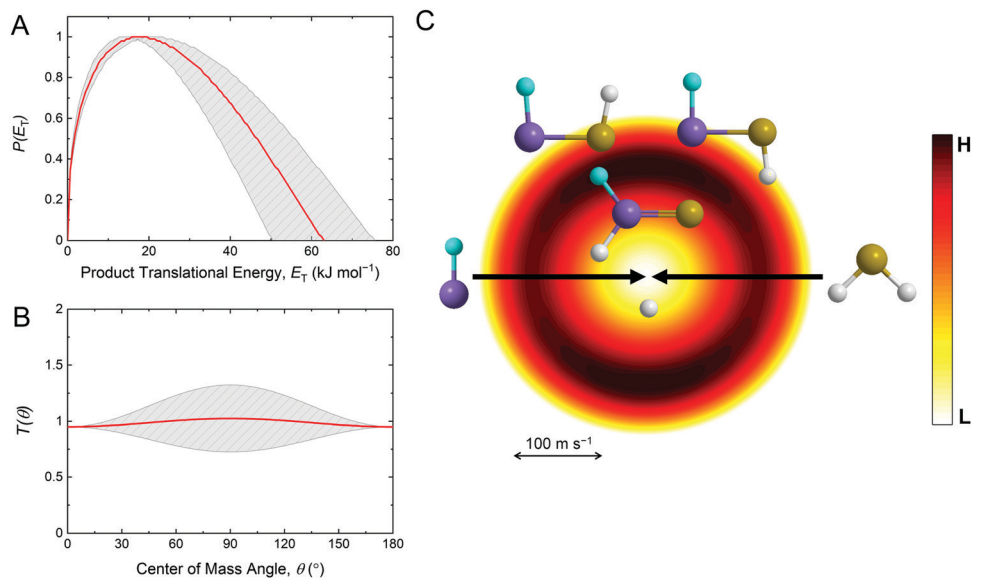

Fig. 9 CM translational energy (A) and angular (B) flux distributions, as well as the associated flux contour map (C) leading to the formation of D1-silanethione (HDSiS) and *trans*/*cis*-D1-thiohydroxysilylene (DSiSH/HSiSD) molecules (m/z = 63) plus atomic hydrogen in the reaction of D1-silylidyne radical (SiD; $X^2\Pi$) with hydrogen sulfide (H_2S). Red lines define the best-fit functions while shaded areas denote the error limits. The flux contour map represents the flux intensity of the reactively scattered products as a function of the product velocity (u) and CM scattering angle (θ), and the color bar indicates the flux gradient from high (H) to low (L) intensity. Atoms are colored as follows: silicon (purple); sulfur (yellow); deuterium (light blue); hydrogen (white).

matching the computed energy of **p1** (-135 ± 4 kJ mol^{-1}); at least for the maximum energy release and reaction energy, **p2** falls outside the error limits. For the D loss channels, these are identical as in the fully deuterated case, with one additional pathway: intermediate **i3** can isomerize by D migration to form **i2′** which can undergo D loss to form **p3′**. Intermediate **i2′** can also be accessed by D migration from **i2** to **i1b′** followed by H migration to **i2′** or rotation isomerization to **i1a′** and H migration to **i2′**. The reaction energy for the D loss channel in the SiD–H_2S system was not obtained experimentally due to the inability to discriminate between the D loss channel and the H loss channel at m/z = 62 (Section 5.2.2). However, for the H loss

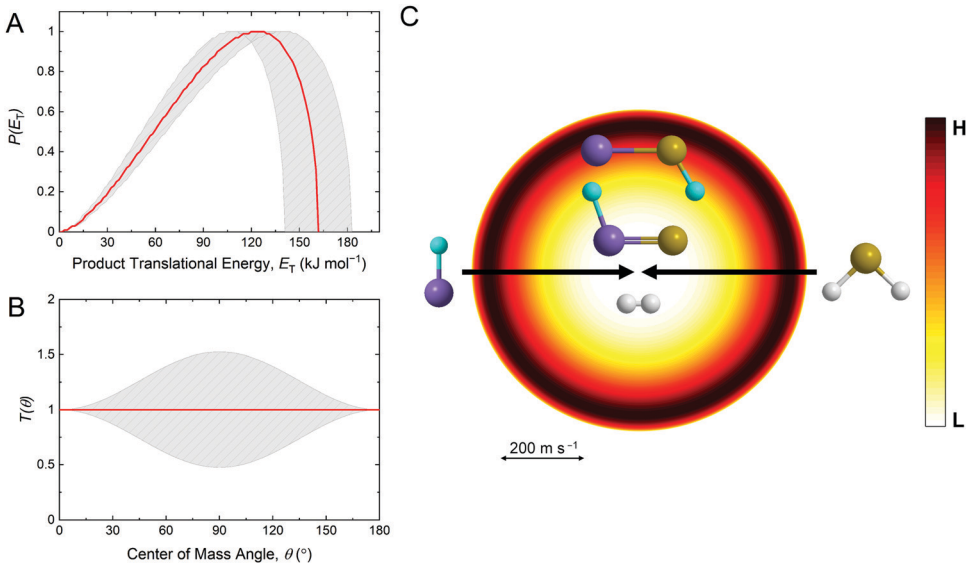

Fig. 10 CM translational energy (A) and angular (B) flux distributions, as well as the associated flux contour map (C) leading to the formation of the D1-(iso)thiosilaformyl (DSiS/SiSD) radical (m/z = 62) plus molecular hydrogen in the reaction of D1-silylidyne radical (SiD; $X^2\Pi$) with hydrogen sulfide (H_2S). Red lines define the best-fit functions while shaded areas denote the error limits. The flux contour map represents the flux intensity of the reactively scattered products as a function of the product velocity (u) and CM scattering angle (θ), and the color bar indicates the flux gradient from high (H) to low (L) intensity. Atoms are colored as follows: silicon (purple); sulfur (yellow); deuterium (light blue); hydrogen (white).

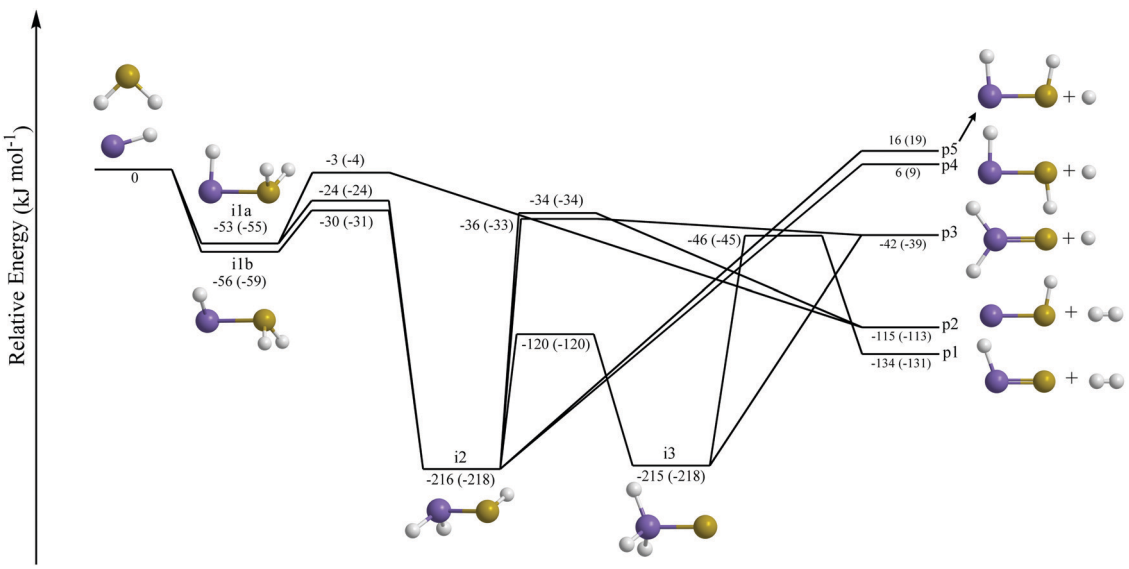

Fig. 11 Potential energy surface for the reaction of the silylidyne radical (SiH; $X^2\Pi$) with hydrogen sulfide (H_2S). Relative energies calculated at the CCSD(T)-F12/aug-cc-pV(T+d)Z//CCSD(T)/aug-cc-pV(T+d)Z + ZPE(M06-2X/cc-pV(T+d)Z) level of theory are shown in kJ mol^{-1}, with calculations for the fully deuterated system shown in parentheses. The surface is simplified by removing barriers, intermediates, and most products above the collision energy of 15.9 kJ mol^{-1}. Atoms are colored as follows: silicon (purple); sulfur (yellow); hydrogen (white).

channel at m/z = 63, the reaction energy of -47 ± 14 kJ mol^{-1} matches well with product **p3** (-44 ± 4 kJ mol^{-1}).

5.4. Astrochemical modeling

The calculated abundances of silanethione (H_2SiS) and the thiosilaformyl radical (HSiS) as well as silicon monosulfide (SiS) and hydrogen sulfide (H_2S) following ice mantle sublimation at t = 0 are shown in Fig. 13 for the O15, OHC, and OPl regions of the Orion Kleinmann-Low nebula. The dark grey boxes represent the observed fractional abundances of silicon monosulfide (SiS) (Table S7, ESI†), whose dominant formation pathway *via* the reaction of atomic silicon with hydrogen sulfide was recently studied by Doddipatla *et al.*[65] These values are defined as the measured column density of silicon monosulfide (SiS) (N(SiS)) divided by that of molecular hydrogen (H_2) (N(H_2)), with errors determined by Tercero *et al.*[75] However,

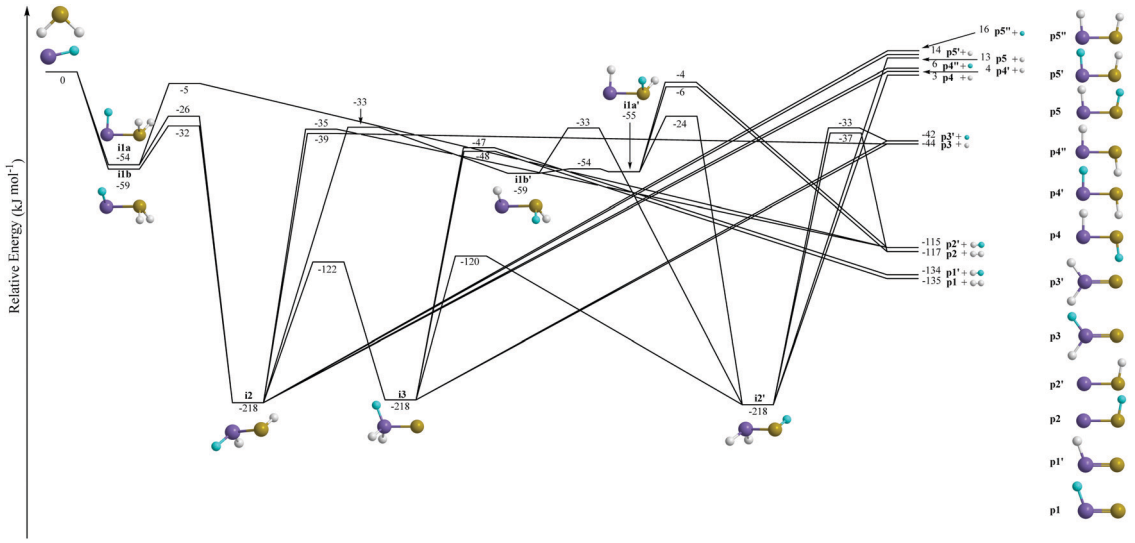

Fig. 12 Potential energy surface for the reaction of the D1-silylidyne radical (SiD; $X^2\Pi$) with hydrogen sulfide (H_2S). Relative energies calculated at the CCSD(T)-F12/aug-cc-pV(T+d)Z//CCSD(T)/aug-cc-pV(T+d)Z+ZPE(M06-2X/cc-pV(T+d)Z) level of theory are shown in kJ mol^{-1}. The surface is simplified by removing barriers, intermediates, and most products above the collision energy of 15.6 kJ mol^{-1}. Atoms are colored as follows: silicon (purple); sulfur (yellow); hydrogen (white); deuterium (light blue).

$N(H_2)$ is difficult to measure accurately, so the light grey area in Fig. 13 reveals the fractional abundance of silicon monosulfide (SiS) with an increase by a factor of three in the error of $N(H_2)$. For times between 10^4 and 2×10^5 years, thought to be typical of the ages of hot molecular cores, the calculated fractional abundance of silicon monosulfide (SiS) is in agreement with the observed values in the OHC and OPl sources. Conversely, the value does not match well in O15, which could imply that the amount of silane and/or hydrogen sulfide released from the ice mantle is a factor of 2–3 times higher than in the other two sources. For the SiH–H_2S system, similar fractional abundances of a few times 10^{-10} for the astronomically still elusive silanethione (H_2SiS) and the thiosilaformyl radical (HSiS) are predicted in OHC and O15, with those in the OPl, the coolest and least dense source, a factor of 2–4 lower. These fractional abundances translate to column densities of $(2–6) \times 10^{13}$ cm^{-2} in OHC and O15 making the detection of both H_2SiS and HSiS feasible since rotational frequencies of H_2SiS[29] and HSiS[76] have been measured. Many rotational transitions of these species have already been covered, and should be searched for, in spectral line surveys of the Orion sources.[75,77,78]

6. Conclusions

First, for the SiD–D_2S system, the crossed molecular beam experiments revealed the existence of the molecular and atomic deuterium loss channels leading to the formation of DSiS and D_2SiS isomer(s). A comparison of the experimentally derived reaction energies with the electronic structure calculations suggest that at least the D1-thiosilaformyl radical (DSiS) (**p1**) and D2-silanethione (D_2SiS) (**p3**) are formed. The reaction mechanism involves indirect scattering dynamics *via* the decomposition of long-lived D_3SiS intermediate(s) involving tight exit transition states both for the atomic and molecular deuterium loss channels; corresponding branching ratios of $43 \pm 8\%$ and $57 \pm 8\%$ were extracted experimentally. Second, for the SiD–H_2S system, the crossed molecular beam experiments exposed the existence of the atomic and molecular hydrogen loss channels leading to the formation of DSiS and HDSiS isomer(s) with possible contributions from an atomic deuterium pathway to H_2SiS. Branching ratios were derived to be $72 \pm 9\%$ and $21 \pm 5\%$ with up to $7 \pm 3\%$ for the atomic deuterium loss. The experimentally extracted energetics of the atomic and molecular hydrogen loss channels support the preparation of at least D1-silanethione (HDSiS) (**p3**) and the D1-thiosilaformyl radical (DSiS) (**p1**) with possible contributions from silanethione (H_2SiS) (**p3′**). As for the SiD–D_2S system, the center-of-mass functions support indirect scattering dynamics *via* the decomposition of long-lived DH_2SiS intermediate(s) involving tight exit transition states. Which are feasible reaction pathways leading to **p1** and **p3**/**p3′**?

For the SiD–D_2S system (Fig. 11), the D1-thiosilaformyl radical (DSiS) (**p1**) can only be formed *via* unimolecular decomposition of intermediate **i3**, *via* molecular deuterium loss through a tight exit transition state located 86 kJ mol^{-1} above the separated products. Intermediate **i3** – the silicon and sulfur isovalent species of the D3-methoxy radical (CD_3O) – can be only accessed *via* deuterium shift from intermediate **i2**; this species represents the isovalent counterpart of the D3-hydroxymethyl radical (CD_2OD). Intermediate **i2** in turn is accessible through a deuterium shift in **i1b** or **i1a**, which can isomerize to one another by bond rotation. Note that the computations could not locate any insertion pathways to form **i2** through insertion of the silicon atom of the SiD radical into the S–D

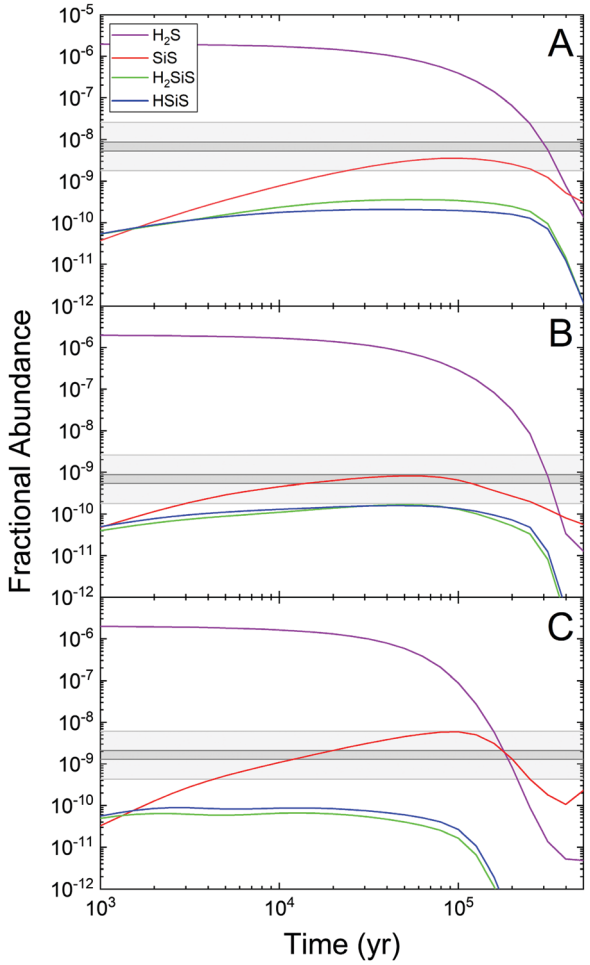

Fig. 13 Time-dependent evolution of the abundances of H_2S, SiS, H_2SiS, and HSiS relative to H_2 in the Orion 15.5 km s^{-1} component (A), Orion Hot Core (B), and Orion Plateau (C) at densities of $n(H_2) = 5 \times 10^5$ cm^{-3}, 5×10^7 cm^{-3}, and 1×10^6 cm^{-3}, and temperatures of 200 K, 225 K, and 125 K, respectively. The grey areas show observed fractional abundances of SiS, with the light grey designating a larger error range for $N(H_2)$.

bond of deuterium sulfide; instead, all approach geometries lead to addition of the SiD radical to the sulfur atom of deuterium sulfide yielding **i1a** or **i1b**. Consequently, the reaction mechanisms leading to the D1-thiosilaformyl radical (DSiS) (**p1**) are initiated by a barrierless addition of the D1-silylidyne radical to one of the non-bonding electron pairs of deuterium sulfide leading to intermediate **i1a** or **i1b**, which may undergo isomerization *via* a Si–S bond rotation to **i1b** or **i1a**, respectively. Two successive deuterium migrations lead from **i1a**/**i1b** to **i3**, which then undergoes molecular deuterium loss through a tight exit transition state to the D1-thiosilaformyl radical (DSiS) (**p1**). Note that in principle, intermediate **i3** could also eject a deuterium atom from the silyl group forming D2-silanethione (D_2SiS) (**p3**). The overall energy of the products of 39 kJ mol^{-1} below the separated reactants is slightly higher than the transition state connecting **i3** and **p1** (−45 kJ mol^{-1}) and hence is competitive. However, the experiments and center-of-mass translational energy distribution proposes a tight exit transition state to form **p3** + D, which is clearly not computed for the unimolecular decomposition of **i3** to **p3** + D. However, the decomposition of intermediate **i2** to **p3** + D involves a somewhat tighter transition state, which correlates qualitatively with the experimental findings. Therefore, we may propose that D2-silanethione (D_2SiS) (**p3**) should form at least through decomposition of intermediate **i2** with possible minor contributions from intermediate **i3**. These aforementioned findings gain full support from the results of the SiD–H_2S system (Fig. 12). Here, the reaction of the D1-silylidyne radical with hydrogen sulfide commences with the barrierless addition of the silicon atom to one of the non-bonding electron pairs of hydrogen sulfide forming intermediate **i1a** or **i1b**, which may isomerize to one another *via* rotation around the Si–S bond. A hydrogen shift results in **i2**, which may lose atomic hydrogen through a tight exit transition state to D1-silanethione (HDSiS) (**p3**). A second hydrogen migration could convert intermediate **i2** to intermediate **i3**, which can emit molecular hydrogen *via* a tight exit transition state forming the D1-thiosilaformyl radical (DSiS).

Overall, our crossed molecular beams experiments of the SiD–D_2S and SiD–H_2S systems merged with electronic structure calculations provided compelling evidence on the formation of the molecular and atomic deuterium loss pathways (SiD–D_2S) and the molecular and atomic hydrogen loss pathways (SiD–H_2S) leading to the D1-thiosilaformyl radical (DSiS) (**p1**) and D2-silanethione (D_2SiS) (**p3**) as well as the D1-thiosilaformyl radical (DSiS) (**p1**) and D1-silanethione (HDSiS) (**p3**) *via* indirect scattering dynamics in barrierless and overall exoergic reactions. The reaction dynamics involve multiple deuterium/hydrogen shifts and tight exit transition states leading to the hitherto astronomically elusive (partially) deuterated versions of the thiosilaformyl radical (HSiS) (**p1**) and silanethione (H_2SiS) (**p3**). Astrochemical modeling suggests further that both silicon-sulfur species should be formed and observable in star forming regions under the premise of a sufficient concentration of silylidyne radicals and readily available hydrogen sulfide. The carbon–oxygen isovalent formyl radical (HCO) and formaldehyde molecule (H_2CO, **1**) have been detected in the Orion Kleinmann-Low nebula,[79] the latter more specifically in the OHC and OPl regions.[80] While HCO and H_2CO have large differences in bond lengths and angles[23] in comparison with their isovalent counterparts HSiS (**p1**) and H_2SiS (**p3**) (Fig. 1), they hold the same point groups and molecular structures. The known dipole moments of these species and rotational transitions in the laboratory suggests that the thiosilaformyl radical (HSiS) (**p1**) and silanethione (H_2SiS) (**p3**) could be detectable in the Orion Kleinmann-Low nebula. In summary, our study provides a look into the complex dynamics of silicon and sulfur chemistry and helps impart insight into silicon- and sulfur-containing molecule formation pathways in deep space.

Conflicts of interest

There are no conflicts to declare.

Acknowledgements

This work at the University of Hawai'i was supported by the US National Science Foundation (CHE-1853541). TJM thanks the UK Science and Technology Facilities Council for support through grant number ST/P000312/1. BRLG also acknowledges the support from the Brazilian funding agencies CAPES, CNPq and FAPEMIG.

References

1 I. Langmuir, *J. Am. Chem. Soc.*, 1919, **41**, 868–934.
2 P. J. Bruna and F. Grein, *Chem. Phys.*, 1992, **165**, 265–279.
3 A. F. Jalbout and A. M. El-Nahas, *THEOCHEM*, 2004, **671**, 125–132.
4 D. Chesnut, *Chem. Phys.*, 2006, **327**, 327–334.
5 X. Liu, X. Liu and X. Wang, *J. Phys. Chem. A*, 2018, **122**, 7023–7032.
6 T. Kudo and S. Nagase, *Organometallics*, 1986, **5**, 1207–1215.
7 M. W. Schmidt, P. N. Truong and M. S. Gordon, *J. Am. Chem. Soc.*, 1987, **109**, 5217–5227.
8 P. v. R. Schleyer and D. Kost, *J. Am. Chem. Soc.*, 1988, **110**, 2105–2109.
9 J. M. Galbraith, E. Blank, S. Shaik and P. C. Hiberty, *Chem. – Eur. J.*, 2000, **6**, 2425–2434.
10 V. G. Avakyan, V. F. Sidorkin, E. F. Belogolova, S. L. Guselnikov and L. E. Gusel'nikov, *Organometallics*, 2006, **25**, 6007–6013.
11 J. X. Chen, D. Liu, C. Zhang, J. Li, H. Zhang and C. K. Kim, *Bull. Korean Chem. Soc.*, 2015, **36**, 123–129.
12 N. N. Greenwood and A. Earnshaw, *Chemistry of the Elements*, Elsevier, 2012.
13 R. Kalescky, E. Kraka and D. Cremer, *Int. J. Quantum Chem.*, 2014, **114**, 1060–1072.
14 W. E. Dasent, *J. Chem. Educ.*, 1963, **40**, 130.
15 P. Davidson and M. Lappert, *J. Chem. Soc., Chem. Commun.*, 1973, 317.
16 N. Wiberg, *J. Organomet. Chem.*, 1984, **273**, 141–177.
17 G. Raabe and J. Michl, *Chem. Rev.*, 1985, **85**, 419–509.
18 L. Pu, B. Twamley and P. P. Power, *J. Am. Chem. Soc.*, 2000, **122**, 3524–3525.
19 H. Suzuki, N. Tokitoh, S. Nagase and R. Okazaki, *J. Am. Chem. Soc.*, 1994, **116**, 11578–11579.
20 S. Thorwirth, J. Gauss, M. C. McCarthy, F. Shindo and P. Thaddeus, *Chem. Commun.*, 2008, 5292–5294.
21 L. Nyulászi, A. Belghazi, S. K. Szétsi, T. Veszprémi and J. Heinicke, *THEOCHEM*, 1994, **313**, 73–81.
22 D.-Y. Hwang, A. M. Mebel and B.-C. Wang, *Chem. Phys.*, 1999, **244**, 143–149.
23 D. E. Woon and E. Herbst, *Astrophys. J., Suppl. Ser.*, 2009, **185**, 273.
24 L. Koziol, Y. Wang, B. J. Braams, J. M. Bowman and A. I. Krylov, *J. Chem. Phys.*, 2008, **128**, 204310.
25 Y. A. Ustynyuk, M. Nechayev, D. Laikov, N. Zemlyanskii, I. Borisova and E. Chernyshev, *Russ. Chem. Bull.*, 2001, **50**, 771–779.
26 J. M. Simmie and J. Würmel, *J. Phys. Chem. Ref. Data*, 2020, **49**, 023102.
27 B. A. McGuire, *Astrophys. J., Suppl. Ser.*, 2018, **239**, 17.
28 F. L. Schöier, J. Bast, H. Olofsson and M. Lindqvist, *Astron. Astrophys.*, 2007, **473**, 871–882.
29 M. C. McCarthy, C. A. Gottlieb, P. Thaddeus, S. Thorwirth and J. Gauss, *J. Chem. Phys.*, 2011, **134**, 034306.
30 P. Thaddeus, M. Kutner, A. Penzias, R. Wilson and K. Jefferts, *Astrophys. J.*, 1972, **176**, L73.
31 P. Schilke, D. Benford, T. Hunter, D. Lis and T. Phillips, *Astrophys. J., Suppl. Ser.*, 2001, **132**, 281.
32 V. L. Fish, *Astrophys. J., Lett.*, 2006, **646**, L57.
33 R. I. Kaiser, A. M. Mebel and Y. T. Lee, *J. Chem. Phys.*, 2001, **114**, 231–239.
34 X. Gu, Y. Guo and R. I. Kaiser, *Int. J. Mass Spectrom.*, 2005, **246**, 29–34.
35 Y. Guo, X. Gu, E. Kawamura and R. I. Kaiser, *Rev. Sci. Instrum.*, 2006, **77**, 034701.
36 N. R. Daly, *Rev. Sci. Instrum.*, 1960, **31**, 264–267.
37 G. O. Brink, *Rev. Sci. Instrum.*, 1966, **37**, 857–860.
38 D. S. Parker, A. V. Wilson, R. I. Kaiser, N. J. Mayhall, M. Head-Gordon and A. G. Tielens, *Astrophys. J.*, 2013, **770**, 33.
39 T. Yang, B. B. Dangi, A. M. Thomas, B. J. Sun, T. J. Chou, A. H. Chang and R. I. Kaiser, *Angew. Chem.*, 2016, **128**, 8115–8119.
40 T. Yang, A. M. Thomas, B. B. Dangi, R. I. Kaiser, M.-H. Wu, B.-J. Sun and A. H. Chang, *J. Phys. Chem. A*, 2016, **120**, 7262–7268.
41 T. Yang, A. M. Thomas, B. B. Dangi, R. I. Kaiser, A. M. Mebel and T. J. Millar, *Nat. Commun.*, 2018, **9**, 1–8.
42 X. Gu, Y. Guo, E. Kawamura and R. I. Kaiser, *J. Vac. Sci. Technol., A*, 2006, **24**, 505–511.
43 W. Bauer, K. H. Becker, R. Düren, C. Hubrich and R. Meuser, *Chem. Phys. Lett.*, 1984, **108**, 560–561.
44 M. F. Vernon, PhD Dissertation, University of California, Berkeley, 1983.
45 P. S. Weiss, PhD Dissertation, University of California, Berkeley, 1985.
46 R. I. Kaiser, *Chem. Rev.*, 2002, **102**, 1309–1358.
47 R. D. Levine and R. B. Bernstein, *Molecular Reaction Dynamics and Chemical Reactivity*, Oxford University Press, USA, 1987.
48 M. W. Schmidt, K. K. Baldridge, J. A. Boatz, S. T. Elbert, M. S. Gordon, J. H. Jensen, S. Koseki, N. Matsunaga, K. A. Nguyen and S. Su, *J. Comput. Chem.*, 1993, **14**, 1347–1363.
49 H. Werner, P. Knowles, G. Knizia, F. Manby, M. Schütz, P. Celani, W. Györffy, D. Kats, T. Korona, R. Lindh, A. Mitrushenkov, G. Rauhut, K. Shamasundar, T. Adler, R. Amos, A. Bernhardsson, A. Berning, D. Cooper, J. Deegan, A. Dobbyn, F. Eckert, E. Goll, C. Hampel, A. Hesselmann, G. Hetzer, T. Hrenar, G. Jansen, C. Köppl, Y. Liu, A. Lloyd, R. Mata, A. May, S. McNicholas, W. Meyer, M. Mura, A. Nicklass, D. O'Neill, P. Palmieri, D. Peng, K. Pflüger, R. Pitzer, M. Reiher, T. Shiozaki, H. Stoll, A. Stone, R. Tarroni, T. Thorsteinsson and M. Wang, *Molpro, Version*

2015.1, a Package of Ab Initio Programs, University of Cardiff, Cardiff, UK, 2015, http://www.molpro.net.
50 W. Kohn and L. J. Sham, *Phys. Rev.*, 1965, **140**, A1133.
51 Y. Zhao and D. G. Truhlar, *Theor. Chem. Acc.*, 2008, **120**, 215–241.
52 T. H. Dunning Jr, K. A. Peterson and A. K. Wilson, *J. Chem. Phys.*, 2001, **114**, 9244–9253.
53 T. H. Dunning Jr, *J. Chem. Phys.*, 1989, **90**, 1007–1023.
54 R. A. Kendall, T. H. Dunning Jr and R. J. Harrison, *J. Chem. Phys.*, 1992, **96**, 6796–6806.
55 P. J. Knowles, C. Hampel and H. J. Werner, *J. Chem. Phys.*, 1993, **99**, 5219–5227.
56 P. J. Knowles, C. Hampel and H.-J. Werner, *J. Chem. Phys.*, 2000, **112**, 3106–3107.
57 T. B. Adler, G. Knizia and H.-J. Werner, *J. Chem. Phys.*, 2007, **127**, 221106.
58 G. Knizia, T. B. Adler and H.-J. Werner, *J. Chem. Phys.*, 2009, **130**, 054104.
59 J. Zhang and E. F. Valeev, *J. Chem. Theory Comput.*, 2012, **8**, 3175–3186.
60 L. M. Ziurys, P. Friberg and W. M. Irvine, *Astrophys. J.*, 1989, **343**, 201–207.
61 J. Martin-Pintado, R. Bachiller and A. Fuente, *Astron. Astrophys.*, 1992, **254**, 315.
62 J. Hatchell, M. Thompson, T. Millar and G. MacDonald, *Astron. Astrophys., Suppl. Ser.*, 1998, **133**, 29–49.
63 J. Hatchell, G. Fuller and T. Millar, *Astron. Astrophys.*, 2001, **372**, 281–290.
64 A. Gusdorf, S. Cabrit, D. Flower and G. P. Des Forêts, *Astron. Astrophys.*, 2008, **482**, 809–829.
65 S. Doddipatla, C. He, S. J. Goettl, R. I. Kaiser, B. R. L. Galvão and T. J. Millar, *Sci. Adv.*, 2021, DOI: 10.1126/sciadv.abg7003.
66 N. R. Crockett, E. A. Bergin, J. L. Neill, C. Favre, P. Schilke, D. C. Lis, T. A. Bell, G. Blake, J. Cernicharo and M. Emprechtinger, *Astrophys. J.*, 2014, **787**, 112.
67 P. N. Brown, G. D. Byrne and A. C. Hindmarsh, *SIAM J. Sci. Statist. Comput.*, 1989, **10**, 1038–1051.
68 E. Herbst and C. M. Leung, *Astrophys. J.*, 1986, **310**, 378–382.
69 D. McElroy, C. Walsh, A. Markwick, M. Cordiner, K. Smith and T. Millar, *Astron. Astrophys.*, 2013, **550**, A36.
70 M. A. Paiva, B. Lefloch and B. R. L. Galvão, *Mon. Not. R. Astron. Soc.*, 2020, **493**, 299–304.
71 T. Yang, B. B. Dangi, R. I. Kaiser, K. H. Chao, B. J. Sun, A. H. Chang, T. L. Nguyen and J. F. Stanton, *Angew. Chem., Int. Ed.*, 2017, **56**, 1264–1268.
72 Z. Yang, B.-J. Sun, C. He, S. Goettl, Y.-T. Lin, A. H. Chang and R. I. Kaiser, *J. Phys. Chem. A*, 2021, **125**, 2472–2479.
73 D. Krajnovich, F. Huisken, Z. Zhang, Y. Shen and Y. Lee, *J. Chem. Phys.*, 1982, **77**, 5977–5989.
74 X. Gu, Y. Guo, F. Zhang and R. I. Kaiser, *J. Phys. Chem. A*, 2007, **111**, 2980–2992.
75 B. Tercero, L. Vincent, J. Cernicharo, S. Viti and N. Marcelino, *Astron. Astrophys.*, 2011, **528**, A26.
76 F. X. Brown, S. Yamamoto and S. Saito, *J. Mol. Struct.*, 1997, **413**, 537–544.
77 B. Tercero, J. Cernicharo, J. Pardo and J. Goicoechea, *Astron. Astrophys.*, 2010, **517**, A96.
78 G. Esplugues, B. Tercero, J. Cernicharo, J. Goicoechea, A. Palau, N. Marcelino and T. Bell, *Astron. Astrophys.*, 2013, **556**, A143.
79 G. A. Blake, E. Sutton, C. Masson and T. Phillips, *Astrophys. J.*, 1987, **315**, 621–645.
80 J. G. Mangum, A. Wootten, R. B. Loren and E. J. Wadiak, *Astrophys. J.*, 1990, **348**, 542–556.